Sun, Z., Jian, Z., Stock, J.M., Larsen, H.C., Klaus, A., Alvarez Zarikian, C.A., and the Expedition 367/368 Scientists
Proceedings of the International Ocean Discovery Program Volume 367/368
publications.iodp.org

Data report: major and trace element and Sr-Nd-Pb-Hf isotope composition of three granite clasts from Hole U1501D in the South China Sea (IODP Expedition 367/368/368X)[1]

Susanne M. Straub,[2] Arturo Gomez-Tuena,[3] Michael J. Dorais[4]

[1] Straub, S.M., Gomez-Tuena, A., and Dorais, M.J., 2022. Data report: major and trace element and Sr-Nd-Pb-Hf isotope composition of three granite clasts from Hole U1501D in the South China Sea, IODP Expedition 367/368/368X. In Sun, Z., Jian, Z., Stock, J.M., Larsen, H.C., Klaus, A., Alvarez Zarikian, C.A., and the Expedition 367/368 Scientists, South China Sea Rifted Margin. Proceedings of the International Ocean Discovery Program, 367/368: College Station, TX (International Ocean Discovery Program). https://doi.org/10.14379/iodp.proc.367368.202.2022
[2] Lamont-Doherty Earth Observatory, Columbia University, USA. **smstraub@ldeo.columbia.edu**
[3] Centro de Geociencias, Universidad Nacional Autónoma de México, Mexico.
[4] Department of Geological Sciences, Brigham Young University, USA.

Keywords
International Ocean Discovery Program, IODP, *JOIDES Resolution*, Expedition 367, Expedition 368, Expedition 368X, South China Sea Rifted Margin, Site U1501, Hole U1501D

References (RIS)

MS 367368-202
Received 8 April 2021
Accepted 18 February 2022
Published 27 April 2022

Abstract

During International Ocean Discovery Program Expeditions 367/368/368X, Hole U1501D was cored on the continental shelf (2846 meters below sea level) in the northern South China Sea (SCS). In Hole U1501D, sediments were recovered from 433.5 to 644.3 meters below seafloor (mbsf) and the acoustic basement was penetrated at 598.91 mbsf. The acoustic basement is a stratigraphic boundary at which late Eocene Cenozoic sediments likely unconformably overlay heterolithic Mesozoic sandstones that are intercalated with rare siltstones and subordinate conglomerate with pebble- and cobble-sized igneous clasts of proximal provenance. Here, we present major and trace elements and Sr-Nd-Pb-Hf isotope data of a fine-grained granite pebble, a medium-grained granite cobble, and a porphyritic volcanic pebble. The data show that these clasts are relics of the Mesozoic subduction-related magmatism that was active along the southeast Asian margin prior to the Cenozoic rifting. The Pb isotope composition of the clasts partially overlaps with the enriched Cenozoic mid-ocean-ridge basalt type and intraplate basalts of the SCS. However, the clasts are distinct from the Cenozoic basalt volcanism in Sr-Nd-Hf isotope space. Thus, Sr-Nd-Hf isotope systematics of the Cenozoic basalts might be useful in detecting traces of crustal contamination in the earliest rift basalts of the SCS that may have erupted through the Mesozoic continental basement.

1. Introduction

The key objectives of International Ocean Discovery Program (IODP) Expeditions 367/368/368X were (1) to test scientific hypotheses of continental breakup at the northern South China Sea (SCS) margin in comparison to other nonvolcanic or magma-poor rifted margins and (2) to improve the understanding of the Cenozoic paleoceanographic evolution of the SCS and Southeast Asia (**Larsen et al.**, 2018a). Seven sites were drilled across the northern SCS margin ~470 km south of the China mainland. Four sites (U1499, U1500, U1502, and U1503) are located in the continent–ocean transition zone (COT) in 3764–3868 m water depth, and three sites (U1501, U1504, and U1505) are located on the outer margin high (OMH) in 2816–2919 m water depth (Figure **F1**). The principal goal of the OMH sites was to obtain a record of the Neogene environmental evolution, but information was also sought on the timing of rifting, the rate of extension, and the degree of crustal exhumation through the recovery of prerift to synrift and postrift rock series (**Larsen et al.**, 2018a).

OMH Site U1501 (18°53.0923′N, 115°45.9455′E; 2845.8 meters below sea level [mbsl]) is located on a regional basement high above the modern carbonate compensation depth (CCD) of the SCS (Figure **F1**). The site was drilled to obtain a complete stratigraphic sequence that spanned the entire period from prior to the rifting to the postrift thermal subsidence (**Larsen et al.**, 2018b). A total of 644.3 m of Cenozoic to Mesozoic sediment was penetrated. The acoustic basement, which was reached at ~600 meters below seafloor (mbsf), is a lithostratigraphic boundary where Cenozoic sediments of late Eocene age likely unconformably overlay Mesozoic heterolithic lithified sandstones with subordinate conglomerate and rare siltstones (**Larsen et al.**, 2018b).

The conglomerate also contains pebble- to cobble-sized granitic and volcanic clasts. Mesozoic granitic rocks are widespread along the southeastern margin of the Eurasian South China block, and they seem to be a volumetrically important constituent of prerift continental crustal basement (Yan et al., 2011, 2014, 2010). It is possible that the earliest (late Eocene) rift-related basalts (e.g., basalts from Site U1502) (Figure **F1**) erupted through the crustal basement (Larsen et al., 2018c) and became contaminated. Given the enriched and distinct elemental and isotopic composition of the Mesozoic granitic crust (Yan et al., 2014), the traces of crustal contamination may be detectable in the compositions of these early rift-related basalts and may help distinguish them from the later rift- and spreading-related basalts that erupted through the newly formed oceanic crust (e.g., basalts from Sites U1500 and U1503) (Figure **F1**).

Although the Mesozoic intrusive rocks of the SCS have been analyzed for Sr-Nd-Pb isotope ratios (Yan et al., 2011, 2014, 2010), there are no published Hf isotope ratios to date. The Nd-Hf isotope system, however, is an important tracer of crustal contamination because Nd and Hf isotope ratios are not only distinct in crustal (granite) and mantle-derived (basalt) lithologies but are also less

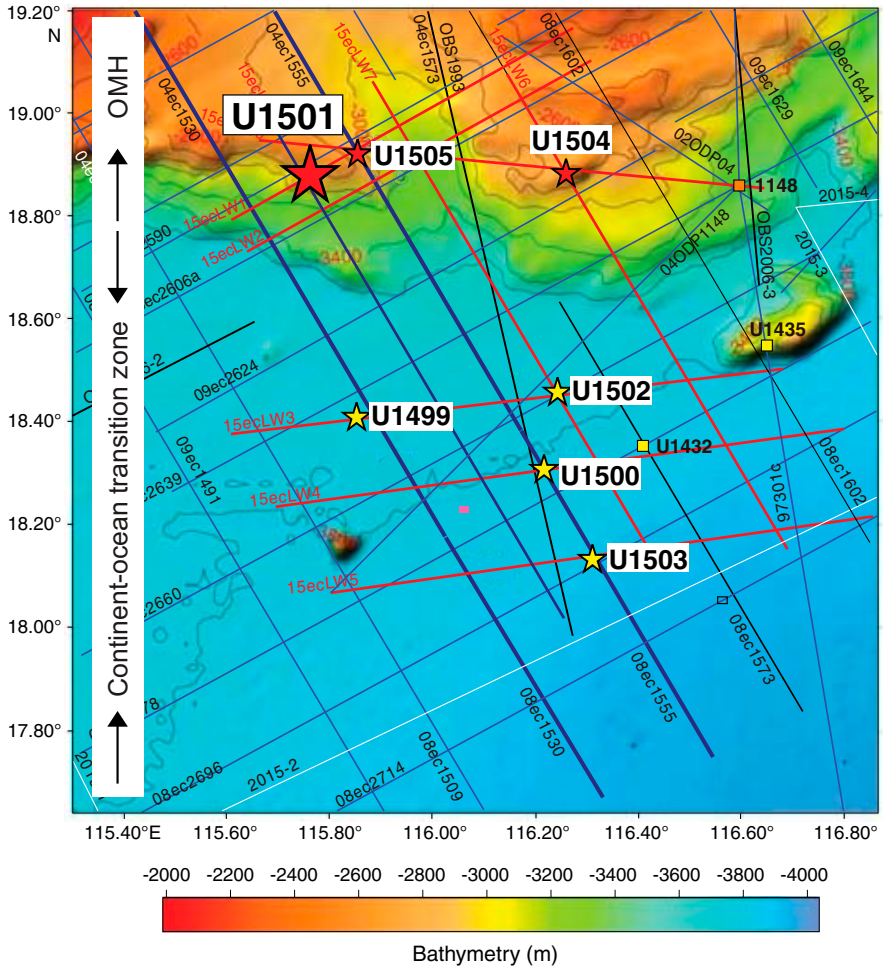

Figure F1. Expedition 367/368/368X drill sites at the northern continental margin of the South China Sea (modified from Larsen et al., 2018a).

sensitive to seawater and hydrothermal alteration that commonly affects nonzero age oceanic basalts. Here, we report new major and trace element and Sr-Nd-Pb-Hf isotope ratio data of n = 3 Mesozoic-age crustal clasts to assess their provenance and their role as potential crustal contaminant of the early SCS rift basalts.

2. Geological setting

2.1. Geological setting of the South China Sea

The geology and evolution of the SCS has been described in detail elsewhere (e.g., **Larsen et al.** [2018a] and references therein; Sun, 2016; Yan et al., 2014). In short, the SCS is a marginal basin to the southwest of the South China block that formed during the Cenozoic by rifting and spreading of the pre-Cenozoic continental lithosphere along the eastern boundary of the Eurasian plate (Sun, 2016). Rifting in the northern SCS Basin started in the late Paleogene and likely continued in the Eocene to the final breakup in the early Oligocene. At around 30–31 Ma (early Oligocene), seafloor spreading began that lasted until ~15 Ma (middle Miocene) (**Larsen et al.**, 2018a; Yan et al., 2014). Miocene-age mid-ocean ridge (MOR)-type basalts were drilled at multiple locations through the SCS (Expedition 349 Scientists, 2014; **Larsen et al.**, 2018a; Zhang et al., 2017, 2018). Oceanic basin volcanism continued after the cessation of spreading (~15 Ma) in the form of younger, late Miocene to Pliocene intraplate volcanoes (young SCS seamounts) that erupted through the mid-ocean-ridge basalt (MORB)-type oceanic lithosphere (Tu et al., 1992; Yan et al., 2008, 2019; Zhang et al., 2017). Since ~15 Ma, the eastern SCS oceanic crust has been subducted along the Manila Trench beneath the Luzon arc.

The knowledge of composition and age of the prerift basement of the SCS is incomplete. It is generally agreed that prior to the SCS Basin formation, the southeastern margin of the Eurasian South China block was an Andean-type subduction zone (e.g., Yan et al., 2011, 2014, 2010) and that its igneous activity may have been related to the long-lasting and widespread Mesozoic (Yanshanian) magmatism in east and southeast China. The Mesozoic igneous activity in the SCS Basin occurred between ~70.5 and 159 Ma, based on granitic rocks found in the Pearl River Mouth Basin and the Zhongsha and Nansha (Spratly Islands) microcontinental blocks. Additional remnants of Mesozoic magmatism are present in the SCS surroundings, which include northern Mindoro (part of the Palawan continental terrane), southeastern Vietnam and its offshore continental shelf, and Borneo (West Kalimantan) (Yan et al., 2014). In addition to the Mesozoic igneous activity, traces of older Paleozoic-age crustal rocks have been found in the Pearl River Mouth Basin (Zhou and Yao, 2009), at Site U1504 (**Straub et al.**, 2022), and on Palawan Island on the conjugate southern continental margin (e.g., Suggate et al., 2014). However, it is not clear how widespread, coherent, and compositionally distinct the Paleozoic rock series may be or whether it has equal potential as crustal basement contaminant as the apparently widespread and voluminous Mesozoic crustal rocks.

2.2. Site U1501 drilling and lithostratigraphy

Two holes were cored at Site U1501. Hole U1501C (18°53.0919′N, 115°45.9485′E; 2846 mbsl) penetrated to 461.8 mbsf and recovered 447.8 m (96.3%) using the advanced piston corer (APC) system. Hole U1501D (18°53.0929′N, 115°45.9370′E; 2846 mbsl) was drilled without coring to 433.5 mbsf and then penetrated to 644.3 mbsf using the rotary core barrel (RCB) system; core recovery was 78.8 m (37.4%).

Lithostratigraphic Units I–III were defined at Site U1501. Units I and II are a 598.91 m thick sequence of Holocene to late Eocene marine sediments that record a gradual uphole trend from a shallow-water (outer shelf or upper continental slope) to a deepwater marine (lower slope) depositional environment and finally to a deep marine environment of a relatively open ocean with rare terrigenous input (**Larsen et al.**, 2018b). The base of Unit II at 598.91 mbsf corresponds to the acoustic basement. The lithologic contact between Units II and III was not recovered but seems unconformable (**Larsen et al.**, 2018b). Moreover, the Unit II/III boundary is characterized by an abrupt lithologic change from the overlying marine sediments to lithified, mostly poorly sorted

feldspar-rich heterolithic sandstones that are interbedded with rare siltstone and poorly sorted conglomerate. Pebble- to cobble-sized clasts include felsic intrusive and volcanic rocks, sedimentary rocks, metamorphic rocks, and rare gabbro. Unit III was likely deposited in a littoral, or nearshore, subaerial fluvial environment where heterolithic clastic components from a larger, proximal catchment area were collected and transported (**Larsen et al.**, 2018b).

3. Methods and materials

3.1. Sample selection and preparation

Because of the small sample volumes of the clasts, shipboard analyses of the clasts were kept to a minimum and included core photography, visual core descriptions (VCDs), and one thin section (Sample 368-U1501D-19R-3, 18–21 cm) (**Larsen et al.**, 2018b). During the postcruise sampling party, a total of four clasts were sampled. Two of these clasts can be visually identified as fine-grained granitic pebble (Sample 19R-3, 14–17 cm) and medium-grained granitic cobble (Sample 20R-2, 40–45 cm). A third clast (Sample 24R-2, 12–16 cm) was macroscopically identified as altered, porphyritic (feldspar) volcanic rock (no thin section was made). The fourth clast (Sample 24R-2, 36–40 cm) was macroscopically tentatively identified as a gabbro. However, the "gabbro" identification could not be verified. The rock was too soft for thin section preparation (T.W. Höfig, pers. comm., 2017), and rock chips disintegrated rapidly to sand during sonication. Thus, this "clast" might have been a highly altered sedimentary rock. Because it was not an igneous rock, this sample was not used beyond obtaining the major and trace element composition listed in Table **T1**.

Chips of the granite/volcanic clasts were sawn from rock. Any saw marks were removed from the rock fragments with sandpaper prior to reducing the fragments to smaller chips by crushing them between two plates of tempered steel. Clean looking rock chips of the sieved 2–4 mm size fraction were then handpicked under the binocular microscope, washed in triple-distilled water and methanol, and powdered in an alumina mortar with pestle for major and trace element and isotope analyses.

3.2. Major and trace elements

Major and trace elements for all three clasts are listed in Table **T1**. Bulk rock major element oxide analyses were completed using X-ray fluorescence (XRF) analysis. XRF preparation included fine crushing in a tungsten-carbide shatterbox. Each sample was dried at 105°C and then calcined in a 1000°C muffle furnace for 4 h to measure loss on ignition (LOI). Lithium metaborate fused glass disks were prepared using an automated Katanax K1 Prime electric furnace. Glass disks were analyzed for major element concentrations (Si, Ti, Al, Fe, Mn, Mg, Ca, Na, K, and P). All XRF analyses were performed at Brigham Young University (Utah, USA) using a Rigaku ZSX Primus II XRF spectrometer operating at 50 kV and 50 mA. Based on repeated analyses of international reference materials, estimates of uncertainty for XRF analysis are ± 1% relative for concentrations above 0.2% for major elements. Bulk rock trace element concentrations were determined using inductively coupled plasma–mass spectrometry (ICP-MS) using a Thermo iCAP-Qc at Centro de Geociencias, Universidad Nacional Autónoma de México (UNAM; Mexico) and following methods previously described by Mori et al. (2007), Gómez-Tuena et al. (2011), and Straub et al. (2015). To ensure dissolution of any refractory phases (e.g., zircon, which was observed in one shipboard thin section), all samples were digested in high-pressure Parr bombs. A precise amount of 50 ± 1 mg of sample powder was weighed in 15 mL Teflon vials, digested overnight in a mixture of 1 mL of concentrated hydrofluoric acid (HF) and 0.5 mL of 8 M HNO_3 at 90°C, and then evaporated to almost dryness. Samples were transferred to 1.5 mL Teflon vials with 1 mL of concentrated HF and 0.5 mL of 8 M HNO_3 and then placed inside the Teflon liner of metal-jacketed Parr pressure bombs, to which 3 mL of a 2:1 HF:8 M HNO_3 mixture was added to equalize the pressure inside and outside the vials and prevent solution loss. The bombs were sealed and heated in an oven at

Table T1. Major element oxides and trace elements concentrations of granite/volcanic clasts, Hole U1501D. **Download table in CSV format.**

190°C for 5 days. After cooling to room temperature, the vials were removed, opened, and placed on a hot plate to evaporate the acids to almost dryness. To decompose any fluoride that might have formed in the previous steps, 1.5 mL of 6 M HCl was added and the vials were heated again in Parr bombs after adding 3 mL of 6 M HCl to the Teflon liner at 190°C in an oven for 24 h. After cooling, the samples were transferred to the original 15 mL vials and evaporated to dryness, after the samples were fluxed twice with 16 M HNO_3. Finally, 2 mL of deionized water and 2 mL of 8 M HNO_3 were added to the samples and the closed vials were left overnight on a hot plate at 90°C.

For analysis, all samples were diluted by a factor of 2000. Samples were corrected for blanks and instrumental drift by internal standards (Ge = 10 ppb; In, Tm, and Bi = 5 ppb) and externally by a highly enriched alkali basalt that was repeatedly analyzed during the run (Sample PS-99-25 from the Palma Sola Massif; Gómez-Tuena et al., 2003). Calibrations, based on international standards JB-2 (Geological Survey of Japan) and BHVO-2, BCR-2, and AGV-2 (U.S. Geological Survey), were strongly linear, and $R^2 \geq 0.999$ for most elements. For all elements, the precision (measured as 1 relative standard deviation of repeat samples) is usually better than 2%, as reported previously (Gómez-Tuena et al., 2011; Mori et al., 2007; Straub et al., 2015).

3.3. Sr-Nd-Pb-Hf isotope ratios of granites/volcanic rock

Sr-Nd-Pb-Hf isotope ratios of the three clasts are listed in Tables **T2** and **T3**. For isotope analyses, ~200 mg of sample powder was leached for 1 h with 6 M HCl at ~100°C prior to digestion in high-pressure Parr bombs as described above. Sr, Nd, Pb and Hf were separated together following the methods described by Mori et al. (2007), Gómez-Tuena et al. (2011), and Straub et al. (2015). Pb was extracted using Dowex AG1X-8 100–200 mesh anion exchange resin and HBr-HCl media, Sr was extracted using Eichrom Sr resin, and Nd was extracted using Eichrom Tru-Spec resin followed by an 0.2 M HNO_3 elution in Eichrom Ln resin (LN-B25-S) using standard separation procedures (Pin et al., 1994). Hf was separated using the single-column method described by Münker et al. (2001).

Sr-Pb-Nd-Hf isotope ratios were analyzed at Centro de Geociencias, UNAM, with a ThermoFisher Neptune Plus multicollector ICP-MS. Sr, Nd, and Pb isotopic compositions of samples and standards were measured in freshly prepared ~200 ppb solutions using wet plasma and a 100 µL/min free aspirating nebulizer. Hf isotopic compositions were measured in freshly prepared ~50 ppb solutions using an Aridus desolvating nebulizer operating at a sample uptake rate of ~50 µL/min for sample introduction. The measured Pb isotopic compositions were exponentially corrected for mass bias by spiking all samples with NIST SRM-997 Tl solution with a reference $^{205}Tl/^{203}Tl$ value of 2.3871, which was added to the samples to match a Pb/Tl ratio of ~4. During the analyses, the average of n = 5 measurements of NIST SRM-981 were $^{206}Pb/^{204}Pb = 16.9314 \pm 0.0011$ (2σ); $^{207}Pb/^{204}Pb = 15.4849 \pm 0.0008$ (2σ); and $^{208}Pb/^{204}Pb = 36.6780 \pm 0.0024$ (2σ). The measured ratios were adjusted to the NIST SRM-981 standard values of $^{206}Pb/^{204}Pb = 16.9356$; $^{207}Pb/^{204}Pb = 15.4891$; and $^{208}Pb/^{204}Pb = 36.7006$ (Todt et al., 1996). The measured $^{143}Nd/^{144}Nd$ ratios were corrected for mass bias to $^{146}Nd/^{144}Nd = 0.72190$. During the analyses, the average of n = 7 measurements of JNdi was $^{143}Nd/^{144}Nd = 0.512089 \pm 0.00006$ (2σ). The measured ratios were adjusted to a JNdi standard of $^{143}Nd/^{144}Nd = 0.512115$ (Tanaka et al., 2000).

The measured $^{176}Hf/^{177}Hf$ ratios were corrected for mass bias using $^{179}Hf/^{177}Hf = 0.7325$. During the analyses, the average of n = 5 measurements of the Hf-Spex standard was $^{176}Hf/^{177}Hf = 0.282151 \pm 0.000003$ (2σ). The measured ratios were further adjusted to $^{176}Hf/^{177}Hf = 0.282160$ of the Hf-Spex standard, which has been intercalibrated with and is considered identical to the JMC-475 standard (Nowell et al., 1998).

Table T2. Measured and initial Sr isotope ratio of medium-grained granitic cobble, Sample 368-U1501D-20R-2, 40–45 cm. **Download table in CSV format.**

Table T3. Measured and initial Nd and Hf isotope ratios of granite clasts, Hole U1501D. **Download table in CSV format.**

The measured $^{87}Sr/^{86}Sr$ ratios were corrected for mass bias to $^{86}Sr/^{88}Sr = 0.1194$ and adjusted to a NIST SRM-987 standard ratio of $^{87}Sr/^{86}Sr = 0.710230$. A problem during multicollector ICP-MS measurements, however, is that critical isobaric interferences of Rb and Kr may occur because Rb may be incompletely removed during column chromatography and Kr is always present as an impurity in the Ar carrier gas, although at extremely low concentrations ($^{82}Kr \leq 0.2$ mV). Although the measured ^{87}Sr, ^{86}Sr, and ^{84}Sr intensities can be corrected to some extent for isobaric Rb and Kr by means of the within-run measurements of ^{85}Rb and ^{83}Kr, the correction may fail in samples with very high Rb/Sr. The latter was the case in two of the Hole U1501D clasts, and $^{87}Sr/^{86}Sr$ could be successfully retrieved only for one clast (Sample 368-U1501D-20R-2, 40–45 cm). The interference-corrected $^{87}Sr/^{86}Sr$ ratios were exponentially normalized for mass bias to $^{86}Sr/^{88}Sr = 0.1194$. During the analyses, the average of n = 5 measurements for NIST SRM-987 were $^{87}Sr/^{86}Sr = 0.710308 \pm 0.00014$ (2σ). The measured ratios were corrected to an NBS-987 standard ratio of $^{87}Sr/^{86}Sr = 0.710230$.

4. Results

4.1. Major and trace elements

The major element oxides and trace elements (Table **T1**) confirm that all three clasts are high-silica (73.3–77.6 wt% SiO_2) igneous rocks that plot in the granite/rhyolite field of the total alkali weight percent versus SiO_2 weight percent (TAS diagram; Middlemost, 1994) (not shown). In the K_2O versus SiO_2 weight percent classification after Le Maitre (1989), they belong to the calc-alkaline to high-K calc-alkaline series. According to the bulk rock classification of Frost et al. (2001), the two granite clasts are ferroan granites (Fe* = 0.78–0.91, where Fe* = FeOt/[FeOt + MgO]), despite the somewhat low Fe* = 0.78 of one sample (368-U1501D-20R-2, 40–45 cm). The modified alkali-lime index (MALI) (Frost et al., 2001) confirms the relation to calc-alkaline rock series. The granite clasts are consistently peraluminous, based either on their aluminum saturation index (ASI) of 1.1–1.2, molar ratio of Al/Ca + 1.67P + Na + K (Frost et al., 2001), or the A/NK (molar Al/[Na + K]) versus A/CNK (molar Al/[Ca + Na + K]) classification diagram of Shand (1943).

The clasts overlap in major and trace elements with the Mesozoic granitic and other intrusive rock (monzogranites, monzonite, tonalites, gabbros, and diorite) that were recovered from the SCS Basin and its broader surroundings (Yan et al., 2014). The similarity with the Mesozoic SCS is strongly apparent in multielement diagrams of incompatible trace elements. In Figure **F2**, the patterns of the three clasts are compared to those of the intrusive rocks (tonalite, monzogranite, and

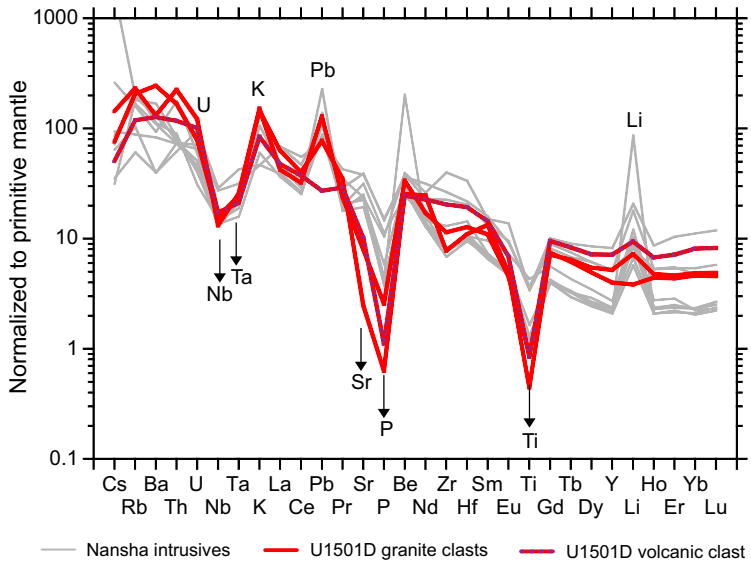

Figure F2. Incompatible trace elements of Hole U1501D granite/volcanic clasts compared to Mesozoic Nansha block intrusive rocks as compiled in Yan et al. (2014), MORB-type Miocene basalts and younger alkaline basalts from Site U1431 in the SCS (Zhang et al., 2017, 2018), and Miocene–Pliocene young SCS seamounts (Yan et al., 2008). Normalized to primitive mantle (McDonough and Sun, 1995).

granodiorite) from the Nansha microblock (~127–159 Ma) on the conjugate southeastern continental margins of the SCS, where the Mesozoic intrusives are best characterized (Yan et al., 2011, 2010). Although the Nansha intrusives are less evolved than the three Hole U1501D clasts, they share similar Ho/Lu ratios (clasts = 2.0 ± 0.2; Nansha granite = 2.1 ± 0.3), which supports their affinity. Moreover, the Nansha intrusives and the three clasts have the same strong relative depletions in Nb, Ta, Sr, P, and Ti and relative enrichments of K and Pb, which are paired with low Nb/La (clasts = 0.32 ± 0.06; Nansha granite = 0.41 ± 0.15) and Ce/Pb (clasts = 8.0 ± 6.5; Nansha granite = 3.6 ± 2.1) and high Th/Nb (clasts = 1.3 ± 0.6; Nansha granite = 0.6 ± 0.3). These characteristics are all typical for subduction-related magmatism worldwide. Preliminary results of monazite age dating for the two granite clasts suggest an age of ~120 Ma (T.W. Höfig, pers. comm., 2017). In summary, the Hole U1501D clasts represent the high-silica Mesozoic southeast Asian continental crustal basement that was split by the SCS Basin formation in the Cenozoic.

4.2. Sr-Nd-Pb-Hf isotope ratios

In the following, isotope data of the Hole U1501D clasts are compared to those of late Mesozoic igneous crust (as compiled by Yan et al., 2014), the MORB-type Cenozoic basalts erupted at IODP Expedition 349 Site U1431 in the central SCS Basin (Zhang et al., 2017, 2018), and younger, Miocene–Pliocene alkaline basalts that were either erupted on-axis at Site U1431 after the termination of the spreading (Zhang et al., 2017, 2018) or from various off-axis seamounts (Yan et al., 2008, 2019). All isotope data are initial ratios, corrected with the ages given in the publications or an age of 120 Ma for the Hole U1501D clasts. Note that no Hf isotope data are available from the SCS Mesozoic crustal basement.

Overall, the initial Sr-Nd-Pb isotope ratio of the Hole U1501D clasts are similar to those of late Mesozoic igneous crust (as compiled by Yan et al. [2014]) (Table **T4**). The single volcaniclast is more radiogenic in Pb isotope ratios and less radiogenic in $^{143}Nd/^{144}Nd$ and $^{176}Hf/^{177}Hf$ than the granite clast, which makes it the most evolved Mesozoic crustal composition known in the SCS. The single granite clast analyzed for $^{87}Sr/^{86}Sr$ is more radiogenic than most of the SCS Mesozoic intrusive rocks; it is still within the range of two other outlying samples of Mesozoic intrusives in the $^{87}Sr/^{86}Sr$ versus $^{143}Nd/^{144}Nd$ space.

4.2.1. Pb isotope ratios

Pb isotope ratios of mantle-derived basaltic magmas are considered to be highly sensitive to crustal contamination. Indeed, the Hole U1501D clasts are more radiogenic in Pb isotopes than the MOR-type basalts of the SCS in the $^{207}Pb/^{204}Pb$ versus $^{206}Pb/^{204}Pb$ diagram (Figure **F3**). However, the initial values of the clasts plot in the $^{208}Pb/^{204}Pb$ versus $^{206}Pb/^{204}Pb$ diagram among the late Miocene to Pliocene (Cenozoic) SCS alkaline basalts erupted at Site U1431 and from the off-axis SCS seamounts (Yan et al., 2015, 2014, 2019). With $^{206}Pb/^{204}Pb$ ratios mostly >18.5 and high average Dupal anomalies of $\Delta 7/4 = 8 \pm 4$ and $\Delta 8/4 = 66 \pm 10$, the late Miocene to Pliocene alkaline basalts are typical of the enriched mantle magmas of Southeast Asia, which may be related either to the Hainan plume or originate enriched lithospheric mantle (e.g., Yan et al., 2018, 2019). Thus, Pb isotope data seem to offer little potential for discriminating between mantle and crustal components in SCS basalts drilled at Sites U1500, U1502, and U1503.

4.2.2. Sr-Nd-Hf isotope ratios

Although Sr, Nd, and Hf isotope ratios of crust and mantle lithologies can also overlap to some extent (e.g., Vervoort et al., 1999, #3279), it appears that their ratios are distinct in the mantle and crustal lithologies of the SCS (Figures **F4**, **F5**). This is primarily attributable to the $^{143}Nd/^{144}Nd$ data, which separates the data fields of the Mesozoic intrusive rocks and the Cenozoic basalts at $^{143}Nd/^{144}Nd = 0.5126$ (approximately bulk silicate earth). There is a small overlap in $^{87}Sr/^{86}Sr$ between the SCS mantle and crustal lithologies, yet in the Nd-Hf isotope space, Hole U1501D clasts are also in their entirety less radiogenic in $^{176}Hf/^{177}Hf$ than the Cenozoic SCS basalts. One tephrite from the late Miocene Zhongnan Seamount (Yan et al., 2008) is strikingly less radiogenic than the bulk of the Cenozoic SCS basalts ($^{176}Hf/^{177}Hf = 0.28288$; $^{143}Nd/^{144}Nd = 0.51268$) and

Table T4. Measured and initial Pb isotope ratios of granite/volcanic clasts, Hole U1501D. **Download table in CSV format.**

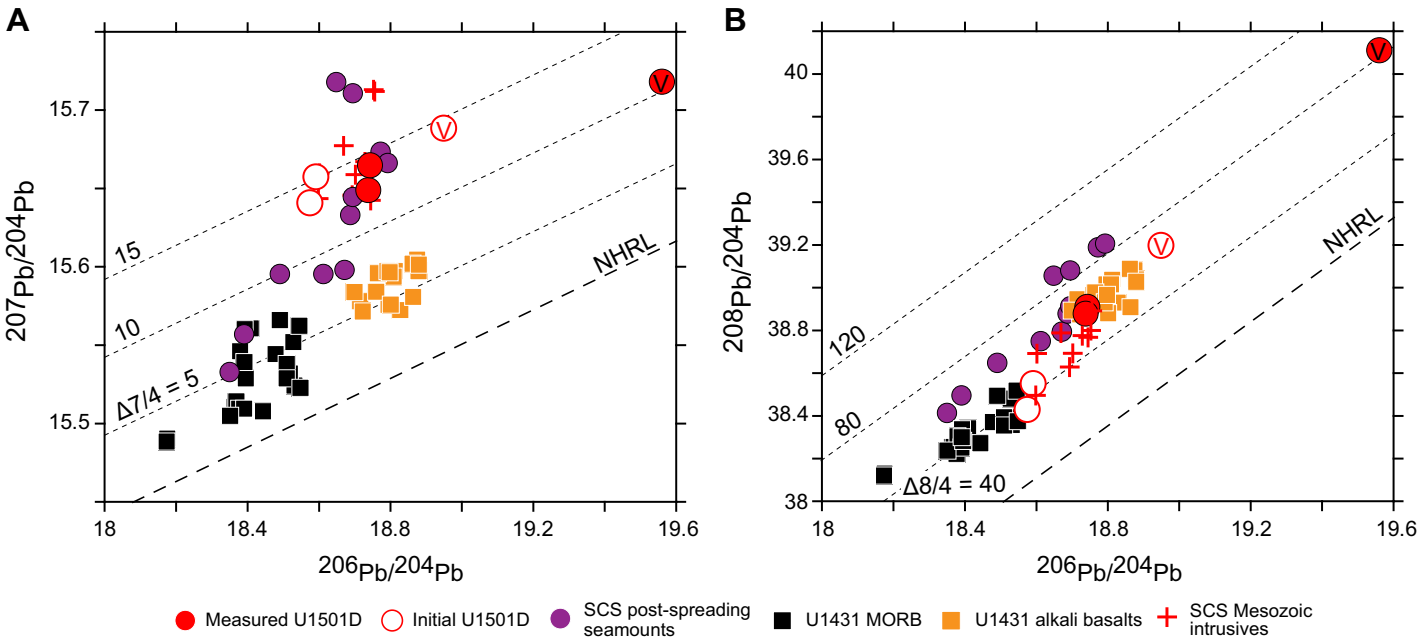

Figure F3. (A) $^{206}Pb/^{204}Pb$ vs. $^{207}Pb/^{204}Pb$ and (B) $^{206}Pb/^{204}Pb$ vs. $^{208}Pb/^{204}Pb$ of Hole U1501D granite/volcanic clasts compared to Mesozoic Nansha block intrusive rocks as compiled in Yan et al. (2014), MORB-type Miocene basalts and younger alkaline basalts from Site U1431 in the SCS (Zhang et al., 2017, 2018), and Miocene–Pliocene young SCS seamounts (Yan et al., 2008). V = volcaniclast (24R-2, 12–16 cm). NHRL = Northern Hemisphere reference line and positive deviations (Δ, "Dupal anomaly") after Dupré and Allègre (1983). All isotope ratios are initial unless otherwise indicated.

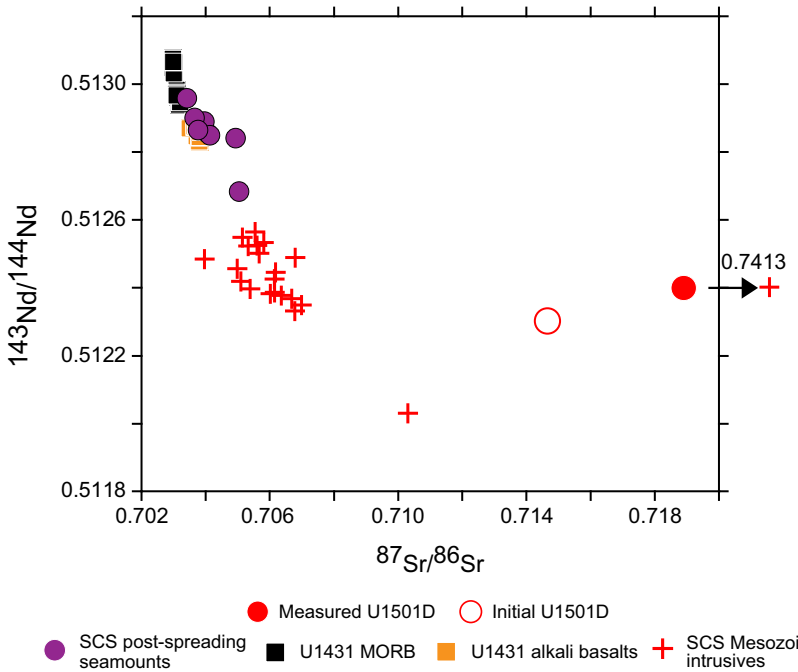

Figure F4. $^{87}Sr/^{86}Sr$ vs. $^{143}Nd/^{144}Nd$ of medium-grained granitic cobble (Sample 368-U1501D-20R-2, 40–45 cm) compared to Mesozoic Nansha block intrusive rocks as compiled in Yan et al. (2014), MORB-type Miocene basalts and younger alkaline basalts from Site U1431 in the SCS (Zhang et al., 2017, 2018), and Miocene–Pliocene young SCS seamounts (Yan et al., 2008). All isotope ratios are initial unless otherwise indicated.

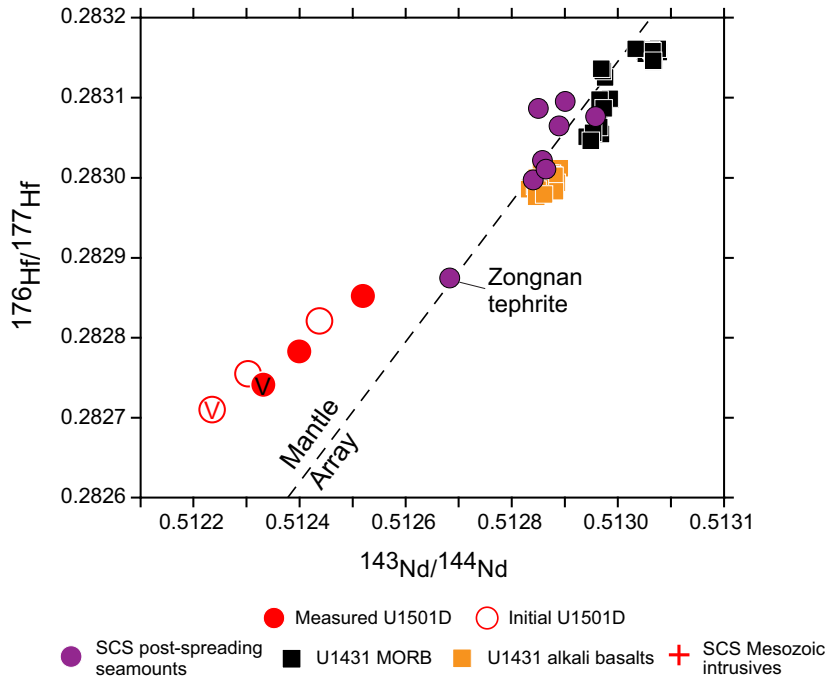

Figure F5. $^{143}Nd/^{144}Nd$ vs. $^{178}Hf/^{177}Hf$ of Hole U1501D granite/volcanic clasts compared to MORB-type Miocene basalts and younger alkaline basalts from Site U1431 in the SCS (Zhang et al., 2017, 2018) and Miocene–Pliocene young SCS seamounts (Yan et al., 2008). V = volcaniclast (24R-2, 12–16 cm). No other Mesozoic intrusives were analyzed for $^{178}Hf/^{177}Hf$. Mantle array after Vervoort et al. (1999).

points to the presence of enriched mantle domains in the SCS mantle. However, even this datum is not as low in $^{143}Nd/^{144}Nd$ and $^{176}Hf/^{177}Hf$ as the Hole U1501D clasts (Figure **F5**).

Additional data in future studies from SCS mantle and crustal lithologies will further test whether the SCS crust and mantle fields are fully separated as outlined with the to-date available data. As of now, Nd-Hf isotope ratios seem best suited to assess the influence of crustal contamination on the early rift basalts, especially given their resistance to modification by seawater and hydrothermal alteration that affected the rift-related SCS Cenozoic basalts.

5. Acknowledgments

This research used samples and data provided by the International Ocean Discovery Program (IODP). Funding for this research was provided by U.S. Science Support Program (USSSP) Post-Expedition Activity Award Grants to SMS and MJD. Irina Liu (Lamont-Doherty Earth Observatory), Liliana Corona, and Ofelia Perez-Arvizu (Centro de Geociencias, UNAM) are thanked for their assistance with sample preparation and analysis. The comments of an anonymous reviewer improved the report.

References

Bouvier, A., Vervoort, J.D., and Patchett, P.J., 2008. The Lu–Hf and Sm–Nd isotopic composition of CHUR: constraints from unequilibrated chondrites and implications for the bulk composition of terrestrial planets. Earth and Planetary Science Letters, 273(1):48–57. **https://doi.org/10.1016/j.epsl.2008.06.010**

Dupré, B., and Allègre, C.J., 1983. Pb–Sr isotope variation in Indian Ocean basalts and mixing phenomena. Nature, 303(5913):142–146. **https://doi.org/10.1038/303142a0**

Expedition 349 Scientists, 2014. South China Sea tectonics: opening of the South China Sea and its implications for southeast Asian tectonics, climates, and deep mantle processes since the late Mesozoic. International Ocean Discovery Program Preliminary Report, 349. **https://doi.org/10.14379/iodp.pr.349.2014**

Frost, B.R., Barnes, C.G., Colins, W.J., Arculus, R.J., Ellis, D.J., and Frost, C.D., 2001. A geochemical classification for granitic rocks. Journal of Petrology, 42(11):2033–2048. **https://doi.org/10.1093/petrology/42.11.2033**

Gómez-Tuena, A., LaGatta, A.B., Langmuir, C.H., Goldstein, S.L., Ortega-Gutiérrez, F., and Carrasco-Núñez, G., 2003. Temporal control of subduction magmatism in the eastern Trans-Mexican Volcanic Belt: mantle sources, slab contributions, and crustal contamination. Geochemistry, Geophysics, Geosystems, 4(8):8912. **https://doi.org/10.1029/2003GC000524**

Gómez-Tuena, A., Mori, L., Goldstein, S.L., and Pérez-Arvizu, O., 2011. Magmatic diversity of western Mexico as a function of metamorphic transformations in the subducted oceanic plate. Geochimica et Cosmochimica Acta, 75(1):213–241. **https://doi.org/10.1016/j.gca.2010.09.029**

Larsen, H.C., Sun, Z., Stock, J.M., Jian, Z., Alvarez Zarikian, C.A., Klaus, A., Boaga, J., Bowden, S.A., Briais, A., Chen, Y., Cukur, D., Dadd, K.A., Ding, W., Dorais, M.J., Ferré, E.C., Ferreira, F., Furusawa, A., Gewecke, A.J., Hinojosa, J.L., Höfig, T.W., Hsiung, K.-H., Huang, B., Huang, E., Huang, X.-L., Jiang, S., Jin, H., Johnson, B.G., Kurzawski, R.M., Lei, C., Li, B., Li, L., Li, Y., Lin, J., Liu, C., Liu, C., Liu, Z., Luna, A., Lupi, C., McCarthy, A.J., Mohn, G., Ningthoujam, L.S., Nirrengarten, M., Osono, N., Peate, D.W., Persaud, P., Qiu, N., Robinson, C.M., Satolli, S., Sauermilch, I., Schindlbeck, J.C., Skinner, S.M., Straub, S.M., Su, X., Tian, L., van der Zwan, F.M., Wan, S., Wu, H., Xiang, R., Yadav, R., Yi, L., Zhang, C., Zhang, J., Zhang, Y., Zhao, N., Zhong, G., and Zhong, L., 2018a. Expedition 367/368 summary. In Sun, Z., Jian, Z., Stock, J.M., Larsen, H.C., Klaus, A., Alvarez Zarikian, C.A., and the Expedition 367/368 Scientists, South China Sea Rifted Margin. Proceedings of the International Ocean Discovery Program, 367/368: College Station, TX (International Ocean Discovery Program). **https://doi.org/10.14379/iodp.proc.367368.101.2018**

Larsen, H.C., Jian, Z., Alvarez Zarikian, C.A., Sun, Z., Stock, J.M., Klaus, A., Boaga, J., Bowden, S.A., Briais, A., Chen, Y., Cukur, D., Dadd, K.A., Ding, W., Dorais, M.J., Ferré, E.C., Ferreira, F., Furusawa, A., Gewecke, A.J., Hinojosa, J.L., Höfig, T.W., Hsiung, K.-H., Huang, B., Huang, E., Huang, X.-L., Jiang, S., Jin, H., Johnson, B.G., Kurzawski, R.M., Lei, C., Li, B., Li, L., Li, Y., Lin, J., Liu, C., Liu, C., Liu, Z., Luna, A., Lupi, C., McCarthy, A.J., Mohn, G., Ningthoujam, L.S., Nirrengarten, M., Osono, N., Peate, D.W., Persaud, P., Qiu, N., Robinson, C.M., Satolli, S., Sauermilch, I., Schindlbeck, J.C., Skinner, S.M., Straub, S.M., Su, X., Tian, L., van der Zwan, F.M., Wan, S., Wu, H., Xiang, R., Yadav, R., Yi, L., Zhang, C., Zhang, J., Zhang, Y., Zhao, N., Zhong, G., and Zhong, L., 2018b. Site U1501. In Sun, Z., Jian, Z., Stock, J.M., Larsen, H.C., Klaus, A., Alvarez Zarikian, C.A., and the Expedition 367/368 Scientists, South China Sea Rifted Margin. Proceedings of the International Ocean Discovery Program, 367/368: College Station, TX (Proceedings of the International Ocean Discovery Program). **https://doi.org/10.14379/iodp.proc.367368.105.2018**

Larsen, H.C., Mohn, G., Nirrengarten, M., Sun, Z., Stock, J., Jian, Z., Klaus, A., Alvarez-Zarikian, C.A., Boaga, J., Bowden, S.A., Briais, A., Chen, Y., Cukur, D., Dadd, K., Ding, W., Dorais, M., Ferré, E.C., Ferreira, F., Furusawa, A., Gewecke, A., Hinojosa, J., Höfig, T.W., Hsiung, K.H., Huang, B., Huang, E., Huang, X.L., Jiang, S., Jin, H., Johnson, B.G., Kurzawski, R.M., Lei, C., Li, B., Li, L., Li, Y., Lin, J., Liu, C., Liu, C., Liu, Z., Luna, A.J., Lupi, C., McCarthy, A., Ningthoujam, L., Osono, N., Peate, D.W., Persaud, P., Qiu, N., Robinson, C., Satolli, S., Sauermilch, I., Schindlbeck, J.C., Skinner, S., Straub, S., Su, X., Su, C., Tian, L., van der Zwan, F.M., Wan, S., Wu, H., Xiang, R., Yadav, R., Yi, L., Yu, P.S., Zhang, C., Zhang, J., Zhang, Y., Zhao, N., Zhong, G., and Zhong, L., 2018c. Rapid transition from continental breakup to igneous oceanic crust in the South China Sea. Nature Geoscience, 11(10):782–789. **https://doi.org/10.1038/s41561-018-0198-1**

Le Maitre, R.W., 1989. A Classification of Igneous Rocks and Glossary of Terms: Boston (Blackwell).

McDonough, W.F., and Sun, S., 1995. The composition of the Earth. Chemical Geology, 120(3–4):223–253. **https://doi.org/10.1016/0009-2541(94)00140-4**

Middlemost, E.A.K., 1994. Naming materials in the magma/igneous rock system. Earth-Science Reviews, 37(3–4):215–224. **https://doi.org/10.1016/0012-8252(94)90029-9**

Mori, L., Gómez-Tuena, A., Cai, Y., and Goldstein, S.L., 2007. Effects of prolonged flat subduction on the Miocene magmatic record of the central Trans-Mexican Volcanic Belt. Chemical Geology, 244(3):452–473. **https://doi.org/10.1016/j.chemgeo.2007.07.002**

Münker, C., Weyer, S., Scherer, E., and Mezger, K., 2001. Separation of high field strength elements (Nb, Ta, Zr, Hf) and Lu from rock samples for MC-ICPMS measurements. Geochemistry, Geophysics, Geosystems, 2(12):2001GC000183. **https://doi.org/10.1029/2001GC000183**

Nowell, G.M., Kempton, P.D., Noble, S.R., Fitton, J.G., Saunders, A.D., Mahoney, J.J., and Taylor, R.N., 1998. High precision Hf isotope measurements of MORB and OIB by thermal ionisation mass spectrometry: insights into the depleted mantle. Chemical Geology, 149(3–4):211–233. **https://doi.org/10.1016/S0009-2541(98)00036-9**

Pin, C., Briot, D., Bassin, C., and Poitrasson, F., 1994. Concomitant separation of strontium and samarium-neodymium for isotopic analysis in silicate samples, based on specific extraction chromatography. Analytica Chimica Acta, 298(2):209–217. **https://doi.org/10.1016/0003-2670(94)00274-6**

Shand, S.J., 1943. Eruptive Rocks. Their Genesis, Composition, Classification, and Their Relation to Ore-Deposits with a Chapter on Meteorite: New York (John Wiley & Sons).

Straub, S.M., Mallick, S., Gomez-Tuena, A., and Dorais, M.J., 2022. Data report: major and trace element and Nd-Pb-Hf isotope composition of the Site U1504 metamorphic basement in the South China Sea, IODP Expedition 367/368/368X. In Sun, Z., Jian, Z., Stock, J.M., Larsen, H.C., Klaus, A., Alvarez Zarikian, C.A., and the Expedition 367/368 Scientists, South China Sea Rifted Margin. Proceedings of the International Ocean Discovery Program, 367/368: College Station, TX (International Ocean Discovery Program). **https://doi.org/10.14379/iodp.proc.367368.203.2022**

Straub, S.M., Gómez-Tuena, A., Bindeman, I.N., Bolge, L.L., Brandl, P.A., Espinasa-Perena, R., Solari, L., Stuart, F.M., Vannucchi, P., and Zellmer, G.F., 2015. Crustal recycling by subduction erosion in the central Mexican Volcanic Belt. Geochimica et Cosmochimica Acta, 166:29–52. **https://doi.org/10.1016/j.gca.2015.06.001**

Suggate, S.M., Cottam, M.A., Hall, R., Sevastjanova, I., Forster, M.A., White, L.T., Armstrong, R.A., Carter, A., and Mojares, E., 2014. South China continental margin signature for sandstones and granites from Palawan, Philippines. Gondwana Research, 26(2):699–718. **https://doi.org/10.1016/j.gr.2013.07.006**

Sun, W., 2016. Initiation and evolution of the South China Sea: an overview. Acta Geochimica, 35(3):215–225. **https://doi.org/10.1007/s11631-016-0110-x**

Tanaka, T., Togashi, S., Kamioka, H., Amakawa, H., Kagami, H., Hamamoto, T., Yuhara, M., Orihashi, Y., Yoneda, S., Shimizu, H., Kunimaru, T., Takahashi, K., Yanagi, T., Nakano, T., Fujimaki, H., Shinjo, R., Asahara, Y., Tanimizu, M., and Dragusanu, C., 2000. JNdi-1: a neodymium isotopic reference in consistency with LaJolla neodymium. Chemical Geology, 168(3–4):279–281. **https://doi.org/10.1016/S0009-2541(00)00198-4**

Todt, W., Cliff, R.A., Hanser, A., and Hofmann, A.W., 1996. Evaluation of a ^{202}Pb–^{205}Pb double spike for high-precision lead isotope analysis. In Basu, A., and Hart, S. (Eds.), Earth Processes: Reading the Isotopic Code. Geophysical Monograph, 95: 429–437. **https://doi.org/10.1029/GM095p0429**

Tu, K., Flower, M.F.J., Carlson, R.W., Xie, G., Chen, C.-Y., and Zhang, M., 1992. Magmatism in the South China Basin, 1. Isotopic and trace-element evidence for an endogenous Dupal mantle component. Chemical Geology, 97(1):47–63. **https://doi.org/10.1016/0009-2541(92)90135-R**

Vervoort, J.D., Patchett, P.J., Blichert-Toft, J., and Albarède, F., 1999. Relationships between Lu–Hf and Sm–Nd isotopic systems in the global sedimentary system. Earth and Planetary Science Letters, 168(1):79–99. **https://doi.org/10.1016/S0012-821X(99)00047-3**

Yan, Q., Shi, X., and Li, N., 2011. Oxygen and lead isotope characteristics of granitic rocks from the Nansha block (South China Sea): implications for their petrogenesis and tectonic affinity. Island Arc, 20(2):150–159. **https://doi.org/10.1111/j.1440-1738.2010.00754.x**

Yan, Q., Castillo, P., Shi, X., Wang, L., Liao, L., and Ren, J., 2015. Geochemistry and petrogenesis of volcanic rocks from Daimao Seamount (South China Sea) and their tectonic implications. Lithos, 218–219:117–126. **https://doi.org/10.1016/j.lithos.2014.12.023**

Yan, Q., Shi, X., and Castillo, P.R., 2014. The late Mesozoic–Cenozoic tectonic evolution of the South China Sea: a petrologic perspective. Journal of Asian Earth Sciences, 85:178–201. **https://doi.org/10.1016/j.jseaes.2014.02.005**

Yan, Q., Shi, X., Liu, J., Wang, K., and Bu, W., 2010. Petrology and geochemistry of Mesozoic granitic rocks from the Nansha micro-block, the South China Sea: constraints on the basement nature. Journal of Asian Earth Sciences, 37(2):130–139. **https://doi.org/10.1016/j.jseaes.2009.08.001**

Yan, Q., Shi, X., Metcalfe, I., Liu, S., Xu, T., Kornkanitnan, N., Sirichaiseth, T., Yuan, L., Zhang, Y., and Zhang, H., 2018. Hainan mantle plume produced late Cenozoic basaltic rocks in Thailand, Southeast Asia. Scientific Reports, 8(1):2640. **https://doi.org/10.1038/s41598-018-20712-7**

Yan, Q., Shi, X., Wang, K., Bu, W., and Xiao, L., 2008. Major element, trace element, and Sr, Nd and Pb isotope studies of Cenozoic basalts from the South China Sea. Science in China Series D: Earth Sciences, 51(4):550–566. **https://doi.org/10.1007/s11430-008-0026-3**

Yan, Q., Straub, S., and Shi, X., 2019. Hafnium isotopic constraints on the origin of late Miocene to Pliocene seamount basalts from the South China Sea and its tectonic implications. Journal of Asian Earth Sciences, 171:162–168. **https://doi.org/10.1016/j.jseaes.2018.06.027**

Zhang, G.-L., Chen, L.-H., Jackson, M.G., and Hofmann, A.W., 2017. Evolution of carbonated melt to alkali basalt in the South China Sea. Nature Geoscience, 10(3):229–235. **https://doi.org/10.1038/ngeo2877**

Zhang, G.-L., Sun, W.-D., and Seward, G., 2018. Mantle source and magmatic evolution of the dying spreading ridge in the South China Sea. Geochemistry, Geophysics, Geosystems, 19(11):4385–4399. **https://doi.org/10.1029/2018GC007570**

Zhou, D., and Yao, B., 2009. Tectonics and sedimentary basins of the South China Sea: challenges and progresses. Journal of Earth Science, 20(1):1–12. **https://doi.org/10.1007/s12583-009-0001-8**